

TENSOR RELATIVE PERMEABILITIES: ORIGINS, MODELING AND NUMERICAL DISCRETIZATION

EIRIK KEILEGAVLEN, JAN M. NORDBOTTEN AND ANNETTE F. STEPHANSEN

This paper is dedicated to the memory of Professor Magne S. Espedal

Abstract. For multi-phase flow in porous media, the fluids will experience reduced conductivity due to fluid-fluid interactions. This effect is modeled by the so-called relative permeability. The relative permeability is commonly assumed to be a scalar quantity, even though justifications for this modeling choice seldom are presented. In this paper, we show that the relative permeability can yield preferential flow directions, and that furthermore, these directions may vary as a function of the fluids present. To model these effects properly, the relative permeability should be considered a tensor. As shown in the paper, standard numerical methods cannot simulate tensor relative permeabilities. We therefore propose two new methods to remedy the situation. One scheme can be seen as an attempt to amend traditional methods to handle tensor relative permeabilities. The second scheme is a consistent approach to simulate the tensors. We also present numerical simulations of cases where upscaling leads to tensor relative permeabilities. The results show that the new methods are indeed capable of capturing tensor effects, moreover, they are in very good agreement with fine scale reference solutions.

Key words. porous media, multi-phase flow, tensorial relative permeability, directional dependency, MPFA, discontinuous Riemann problems

1. Introduction

Multi-phase flow in porous media is the governing physics for many natural and artificially constructed systems. Natural systems of interest are of both geologic and biologic character, while artificial systems pertain primarily to engineered materials. Controlling fluid flow in complex porous media is consequently of great practical importance. While single-phase flow is fundamentally well understood, flow of multiple fluid phases still provides challenges for modeling and simulation. Herein we address the challenge when the material has a preferential direction of conductance, and when this direction may be fluid fraction dependent at the modeling scale.

It is common in experiments and modeling to consider the anisotropic nature of intrinsic permeability. This is understood physically as resulting from subscale structuring of the porous media itself. In both natural and artificial porous media the finest scale at which Darcy's law is applicable is often referred to as the Representative Elementary Volume (REV). However, even the REV scale will often contain structure on the finer scale which is the pore-space itself. When this structure is expressed as layering, or channeling, fluid flow will be preferential in some directions, which is parameterized as an anisotropic permeability. Textbook examples are wood (channeling) and geological media (layered at all scales due to compaction).

It is natural to assume that this subscale structure will also impact the fluid distribution when two or more fluids are present simultaneously in a porous media. Such a subscale structure in fluid distribution may well alter the effective anisotropy.

The multi-fluid flow properties of porous media can be parameterized by the so-called relative permeability functions. From our discussion, we are tempted to state that these relative permeability functions are anisotropic, with anisotropy ratio and direction that may both be functions of saturation. However, common modeling almost universally neglects this aspect, with the a-priori assumption that the anisotropy ratio is independent of saturation.

Several previous studies have shown that the relative permeability function may be anisotropic at scales ranging from the REV scale [12], through the laboratory scale [15], to the field scale [26, 27, 24]. Furthermore, in these studies it is frequently observed that a full description of relative permeability give significant qualitative differences from scalar models.

The aim of this contribution is therefore two-fold: Firstly, to highlight mechanisms that cause saturation-dependent anisotropy at all scales. Secondly, to propose numerical approaches that adapt to the significant challenges this saturation dependence causes in practical modeling.

In this paper, we begin to address both these points. In Section 2, we discuss the understanding that exists regarding relative permeability (in the continuation, we will always imply that relative permeability is anisotropic, unless otherwise stated). In particular, we show using a network flow model how anisotropy arises even at the finest continuum scale, and subsequently consider the emergence of anisotropy in relative permeability from upscaling procedures. In Section 3, we highlight some of the main challenges that arise from a simulation perspective with a full description of relative permeability, using IMPES time-stepping with control-volume spatial discretization as a backdrop for our discussion. Acknowledging these difficulties, in Section 4 we propose ideas for handling the full tensors within the traditional numerical framework, as well as an approach that allows for the saturation equation to be solved consistently. Section 5 combines the work of the preceding sections within numerical implementations. These illustrate A) Flow patterns that are unique to full relative permeability systems and B) The performance of our proposed solution approaches. The paper is concluded in Section 6.

2. The nature of relative permeability

While the permeability of a porous material is almost universally modeled as anisotropic, relative permeability is consistently modeled as a scalar function of saturation (see e.g. [20, 11]). Notable exceptions exist (see e.g. [12, 26, 27, 24, 10]), however these references usually consider anisotropy in relative permeability as a consequence of upscaling, rather than intrinsic to the porous media itself. In this section, we will argue that relative permeability should be modeled as anisotropic at all scales, by considering firstly the finest scale at which Darcys law is applied (the REV scale). Subsequently, we will consider anisotropic relative permeability as it arises from upscaling vertically segregated systems.

To be concrete, we establish the following definitions relating to permeability:

- The intrinsic permeability \mathbf{K} is the permeability of a porous medium saturated by one fluid.
- The effective permeability \mathbf{K}_α , with respect to a fluid phase α , is the permeability of a porous medium as experienced by that fluid.
- The relative permeability $\mathbf{K}_{r,\alpha}$, is the ratio of the effective to the intrinsic permeability. In the case where the two latter are tensors, the relative permeability can be defined as $\mathbf{K}_{r,\alpha} = \mathbf{K}_\alpha \cdot \mathbf{K}^{-1}$.

We make the following four comments on these definitions. Firstly, the intrinsic and effective permeabilities are usually argued from Onsager’s principle to be symmetric and non-negative definite matrices. Secondly, it is important to note that this implies that the derived quantity relative permeability need not be symmetric, nor non-negative definite. Thirdly, the relative permeability could also be defined by reversing the order of intrinsic and effective permeability in its definition. The order chosen here is consistent with the upscaling to Darcy’s law from the pore scale (see next section). Finally, in the case where the main directions of effective permeability are not dependent on saturation, the relative permeability can be defined component by component, and need not be defined through the matrix multiplication.

2.1. The REV scale. Numerous investigators have considered the relationship between Navier-Stokes equations at the scale of porous grains and the smallest scale of which Darcy’s law can be applied. Among the earliest, and still most common ways to probe this relationship is through the use of averaging methods (for an overview of these approaches, see [21]). With these approaches, even for homogeneous porous media one arrives at relationships of the form (see e.g. [23, 21]):

$$(1) \quad \nabla p - \rho_\alpha \mathbf{g} = -\mathbf{R}(\mathbf{r}_r^{\alpha,\alpha} \mathbf{q}_\alpha + \mathbf{r}_r^{\alpha,\beta} \mathbf{q}_\beta).$$

Here, \mathbf{R} refers to the intrinsic resistivity of the medium, p is pressure, \mathbf{g} the gravitational vector, ρ_α is the density of phase α , and \mathbf{q}_α and \mathbf{q}_β are the velocities of phase α and β , respectively. We see the viscous cross-coupling between the fluids explicitly represented by the presence of fluid β in the equation. The coefficients of relative resistivity $\mathbf{r}_r^{\alpha,\beta}$ and $\mathbf{r}_r^{\alpha,\alpha}$ are usually considered as scalars without further comment. However, it is clear from their origins as approximations to surface integrals representing shear forces, that they can only be scalars if the sub-scale fluid distribution is isotropic. The validity of this hypothesis is by no means self-evident.

From Equation (1), we obtain the traditional form of the two-phase extension of Darcy’s law by multiplying the equation with the intrinsic and relative permeabilities, which gives rise to the ordering used in the definition of the relative permeability. In absence of cross-coupling terms, this leads to

$$-\mathbf{K}_{r,\alpha} \mathbf{K}(\nabla \mathbf{p} - \rho_\alpha \mathbf{g}) = \mathbf{q}_\alpha.$$

Here we have defined the permeability $\mathbf{K} = \mathbf{R}^{-1}$ and the relative permeability $\mathbf{K}_{r,\alpha} = (\mathbf{r}_r^{\alpha,\alpha})^{-1}$.

Current models for construction of virtual porous rocks apply a process-dependent approach, where the primary components are A) Simulated sedimentation under gravitational forces, and B) Simulated compaction in the direction of gravity [6]. This mimics how real geological porous media are formed. We see that during both stages of the construction of a porous media, directional dependence along the gravitational vector is introduced, and indeed this is the primary reason why intrinsic permeability is considered anisotropic. Furthermore, we understand intuitively that the compaction process will also lead to systematic anisotropy in pore geometry, such that pore throats oriented parallel to gravity may have different cross-sectional properties (area and geometric factor) than pore throats oriented perpendicular to gravity. This anisotropy in pore geometry becomes important, as it is generally thought that it is the pore throats that govern the percolation

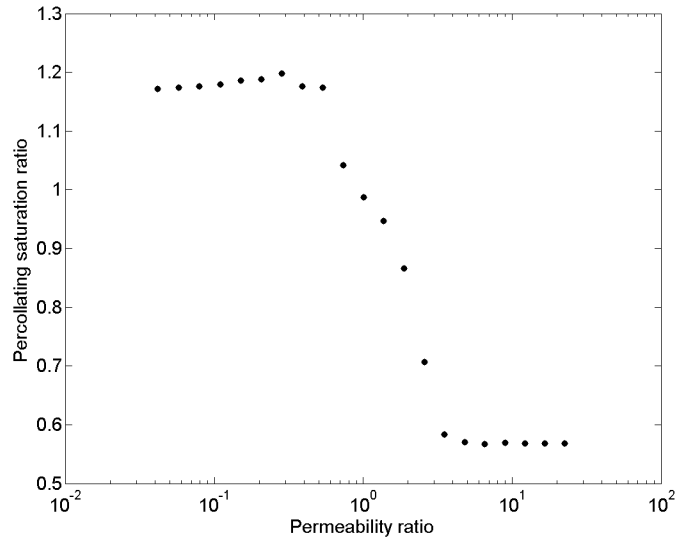


FIGURE 1. Correlation between anisotropy ratio of intrinsic permeability and ratio of directionally dependent percolating saturation, calculated from a network model of porous media.

threshold for porous media [17]. Therefore, it may be expected that fluid percolation has a preferred direction. This immediately implies an anisotropic relative permeability at saturations that fall between the percolation thresholds, where the relative permeability is non-zero only in the direction(s) of fluid percolation. Consequently, we note that for each fluid separately, there may arise a situation where the effective (and relative) permeability of the fluid has an infinite anisotropy ratio. In addition, we note that numerical representations such as network models are often used for calculating relative permeability. This implies that the relative permeability is evaluated based on the directional flow in the network.

While directional calculations may in some cases yield identical results, this will in general not hold [7]. Here, we illustrate this by simulations conducted on a network with a regular cubic structure of dimensions 30^3 nodes. The pore throat radii are given by a truncated log-normal distribution, where we have introduced a directional anisotropy in the mean log-normal pore radii. The results are plotted in Figure 1, where we show the resulting anisotropy ratios for permeability along the horizontal axis, and the anisotropy in percolation threshold (as obtained by percolation analysis for the non-wetting fluid) along the vertical axis. Anisotropy values greater than unity refer to a layered porous media, while values less than one indicate porous media. The scattering in the data is due to the random selection of pore-throat radii in the network.

We see that anisotropy in intrinsic permeability is strongly correlated to anisotropy in percolating saturation, and thus also to effective and relative permeability. Based on the above discussion, we argue that relative permeability should in general be considered as an anisotropic quantity, even at the finest scale of resolution: the representative elementary volume.

2.2. Capillary based upscaling. The balance between capillary and viscous forces indicate that for most geological flows, capillary equilibrium can be assumed

for the purposes of upscaling at the smaller scales. In a little-cited paper, Corey and Rathjens used this approach already as early as 1956 to show how this leads to anisotropic relative permeability [12]. Their paper gives a very instructive approach to understanding how upscaling can lead to anisotropic relative permeability, and we will review a generalized form of their main argument here. We consider a layered media. For simplicity, let the layering consist of two types of porous rock, indexed by $i = \{1, 2\}$. We consider non-hysteretic capillary pressure-saturation functions for the two materials

$$p_i^{cap}(s_i) = p_{n,i} - p_{w,i}.$$

Here n indicates the non-wetting phase and w the wetting phase. In this and the next section, we will use small letters for fine-scale variables and parameter functions, while we will reserve the use of capital letters for the upscaled relationships.

It is physically reasonable to assume that p_i^{cap} is invertible, such that we can define its inverse function $s_i^{cap}(p_i^{cap})$ for both materials. Then, assuming capillary equilibrium between the two materials, $p_1^{cap}(s_1) = p_2^{cap}(s_2)$, we see that we have the relation

$$s_2 = s_2^{cap}(p_1^{cap}(s_1)).$$

Denoting further the volumetric fractions of the void space as ω_1 and ω_2 , where $\omega_1 + \omega_2 = 1$, we have that the total saturation can be expressed as $S = \omega_1 s_1 + \omega_2 s_2$, and thus the individual saturations are defined implicitly from the total saturation through the relations

$$\omega_1 s_1 = S - \omega_2 s_2^{cap}(p_1^{cap}(s_1)), \quad \omega_2 s_2 = S - \omega_1 s_1^{cap}(p_2^{cap}(s_2)).$$

We now recall that for a layered media, the correct effective permeabilities can be found by taking the harmonic average normal to the layering and the arithmetic average parallel to the layering. For simplicity, let the two materials have the same intrinsic properties, and isotropic relative permeabilities. Thus the intrinsic properties of the compound (upscaled) material are identical to those of its components, while it follows that the upscaled relative permeability is anisotropic, with principal components

$$K_r^{\parallel} = \omega_1 k_{r,1}(s_1) + \omega_2 k_{r,2}(s_2), \quad K_r^{\perp} = [\omega_1 k_{r,i}^{-1}(s_1) + \omega_2 k_{r,i}^{-1}(s_2)]^{-1}.$$

Note that in the interest of keeping the notation simple, we have omitted the designation of fluid phase, since the expressions are identical for both fluid phases. Due to the general properties of arithmetic and harmonic averages, we have that the relative permeability in the parallel direction will always exceed that of the perpendicular direction, $K_r^{\parallel} \geq K_r^{\perp}$. By specification of parameters ω_i , and the parameter functions $k_{r,i,j}(s_i)$ and $p_i^{cap}(s_i)$ for both materials i and both phases j , we can evaluate the upscaled relative permeabilities, and assess the importance of anisotropy. Note that the upscaled relative permeability can be anisotropic, even if only the capillary pressure functions, or the relative permeability functions, are different between the two materials. Since both of these origins to anisotropy are saturation dependent and thereby varying during a two-phase simulation, the anisotropy effect cannot be lumped into the absolute permeability, which is constant.

As an illustration, we consider $\omega_i = .5$, and a phase where the relative permeabilities are given as quadratic and cubic, respectively, e.g. $k_{r,i} = s_i^{i+1}$. We give the capillary pressure for the two materials in terms of the saturation-capillary relationship as $s_1^{cap}(p_1^{cap}) = (\text{erf}(-p_1^{cap}) + 1)/2$ and $s_2^{cap}(p_2^{cap}) = (\text{erf}(-2p_2^{cap}) + 1)/2$. The isotropic relative permeabilities of the two materials, together with the principal

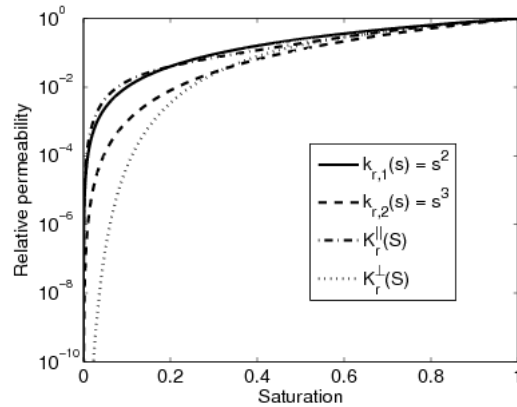


FIGURE 2. Anisotropic relative permeabilities as calculated for a layered porous medium in capillary equilibrium. For comparison, the relative permeabilities of the individual layers is also shown.

components of the anisotropic upscaled relative permeability, are plotted in Figure 2.

We make the interesting observation that we introduced no large material heterogeneity (the capillary pressure functions differ by a factor two, and the relative permeability functions are similar). Nevertheless, the upscaled relative permeability functions exhibit interesting features. In particular, we see that due to the different saturations in the two materials, for small saturations the parallel upscaled relative permeability (as a function of the averaged saturation), may exceed that of either material, while the opposite remains true for the perpendicular direction. Indeed, the anisotropy ratio becomes unbounded as the saturation vanishes, exceeding 10 at $S = 0.2$ and 300 at $S = 0.1$.

2.3. Vertically segregated upscaling. In this subsection we aim at illustrating relative permeability at a larger scale, and also introduce saturation-dependent anisotropy directions. We will therefore review how relative permeabilities appear in vertically integrated models, which result from appropriate upscaling for vertically segregated systems [28]. In the simplest vertically integrated models, gravity is considered to dominate viscous and capillary forces. Therefore, it is expected that the fluids segregate according to density, and the transition zone between the fluids is considered negligible [20]. In this setting, the upscaled effective permeability for the integrated (upscaled) model simply becomes the integral over a vertical segment in an aquifer. For concreteness, we consider the densest phase, assuming no residual saturations (e.g. no dependence on the fine-scale relative permeability), for which the upscaled relative permeability is defined as

$$\mathbf{K}_r \equiv \int_0^{SH} \mathbf{k}_{\parallel}(z) dz \cdot \mathbf{K}^{-1}.$$

Here, the upscaled intrinsic permeability is simply the integral of the fine-scale permeability across the vertical extent of the porous formation,

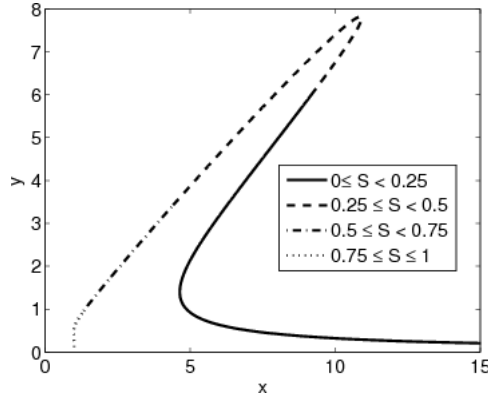


FIGURE 3. Principal direction and anisotropy ratio of effective permeability in a vertically integrated model. The line is parameterized by the saturation of the coarse model. The distance from the origin gives the anisotropy ratio, while the angle from the x -axis on the figure gives the rotation of the major principal axis of the tensor from the x -axis in the domain.

$$\mathbf{K} \equiv \int_0^H \mathbf{k}_{\parallel}(z) dz.$$

In the above equations, H denotes the vertical extent of the formation, while $S = s/H$ is the integral saturation of the denser fluid. The subscript \parallel on the fine-scale permeability denotes the components parallel to flow (e.g. perpendicular to averaging direction). A heterogeneous nature of the fine-scale permeability will now give rise to anisotropy in relative permeability.

As an example, let the horizontal component (projection onto the xy -plane) of the fine scale intrinsic permeability be given by

$$(2) \quad \mathbf{k}_{\parallel}(z) = \begin{pmatrix} \frac{\gamma_1}{H} & \frac{\gamma_2}{H} \sin(2\pi z/H) \\ \frac{\gamma_2}{H} \sin(2\pi z/H) & \frac{3}{2H} \left(\frac{z}{H}\right)^{1/2} \end{pmatrix},$$

where $0 \leq \gamma_1$ and γ_2 is defined such that the matrix is always positive definite. This corresponds to a case where the main direction of anisotropy rotates when moving along a vertical direction in the reservoir. Then a simple calculation shows that the upscaled permeability is simply $K = \text{diag}(\gamma_1, 1)$, and for the case of $\gamma_1 = 1$ it is the (isotropic) identity matrix, while the relative permeability becomes anisotropic and given by

$$(3) \quad \mathbf{K}_r(S) = S \cdot \begin{pmatrix} 1 & \frac{\gamma_2}{2\pi S} [1 - \cos(2\pi S)] \\ \frac{\gamma_2}{2\pi \gamma_1 S} [1 - \cos(2\pi S)] & S^{1/2} \end{pmatrix},$$

Despite its somewhat pathological construction, this example is instructive, in that it firstly shows that the relative permeability need not be symmetric (when $\gamma_1 \neq 1$). Secondly, setting $\gamma_1 = 1$, we note that the effective (which is now equal to the relative) permeability can be anisotropic, even when the (upscaled) permeability is isotropic. This is highlighted in Figure 3, where we show the principal

component of the relative permeability tensor (scaled by the magnitude of the secondary component) in a phase plane. Thus the anisotropy ratio for given S can be found from the figure as the distance from the origin at the point of the curve corresponding to that saturation. Similarly, the rotation of the major principal axis of the tensor relative to the x -axis in the domain is in the figure represented as the angle of points of the curve relative to the x -axis in the figure. We see that for low saturations, the anisotropy ratio is high (in fact, it approaches infinity as $S \rightarrow 0$), and the major principal axis of the relative permeability is almost aligned with the x -axis. As the saturation increases, the anisotropy direction and ratio vary according to the figure. At $S = 1$, the relative permeability is isotropic and equal to 1. Again we see that the anisotropy is a function of saturation, thus it cannot be modeled by the intrinsic permeability.

3. Model Equations

In this section we look at traditional discretization schemes and some of the challenges that arise when introducing tensorial relative permeabilities. For simplicity we study the flow of two immiscible, incompressible phases denoted water and oil. Capillary and gravitational forces are neglected. The transport equation for a phase α can then be written [11]

$$\frac{\partial S_\alpha}{\partial t} - \nabla \cdot \mathbf{q}_\alpha = Q_\alpha.$$

The phase flux is given by the two-phase version of Darcys law,

$$(4) \quad \mathbf{q}_\alpha = -\mathbf{\Lambda}_\alpha \mathbf{K} \nabla p.$$

In these equations, we have used the phase mobility defined as $\mathbf{\Lambda}_\alpha = \mathbf{K}_{r,\alpha} / \mu_\alpha$. The volumetric sources for phase α are represented by Q_α . The flow is modeled as incompressible, thus $\nabla \cdot \mathbf{q}_T = 0$, where \mathbf{q}_T is the total velocity field. Since the fluids fill the total pore volume the saturations must sum to one, i.e. $S_w + S_o = 1$. By summing the transport equations for the two phases, and applying incompressibility of the phases, we get a pressure equation

$$(5) \quad -\nabla \cdot (\mathbf{\Lambda}_T \mathbf{K} \nabla p) = Q_T,$$

where $\mathbf{\Lambda}_T$ is the total mobility, and Q_T is the total source term. The transport solve should be based on the total velocity field, since it is a smoother function of time than the phase velocities. By combining Darcys law for phase and for the total velocity, we find the fractional flow formulation $\mathbf{q}_\alpha = \mathbf{\Lambda}_\alpha \mathbf{\Lambda}_T^{-1} \mathbf{q}_T$, and this gives us the transport equation

$$(6) \quad \frac{\partial S_\alpha}{\partial t} - \nabla \cdot (\mathbf{\Lambda}_\alpha \mathbf{\Lambda}_T^{-1} \mathbf{q}_T) = Q_\alpha.$$

Note that $\mathbf{\Lambda}_\alpha \mathbf{\Lambda}_T^{-1}$ can be considered a tensor fractional flow function. Our numerical approximations will be based on the Equations (5) and (6). We remark that except from the tensorial relative permeability, the equations given here are identical to the standard equations for two phase flow.

3.1. Challenges for traditional discretizations. To discretize the governing equations we apply control volume methods, which are the prevailing schemes used in industrial reservoir simulation. Moreover, we will discuss only the IMPES formulation, in which the pressure equation is first solved implicitly in time, and then the transport equation is solved explicitly using the new pressure field. The difficulties that arise from the saturation dependent tensors are also valid for other time stepping schemes. We first consider the single phase pressure equation, which is found by setting the relative permeability in Equation (5) equal to the identity matrix. Control volume methods integrate the equation over each grid cell and uses continuous fluxes so that mass is conserved locally. The fluxes are obtained as a discrete form of Darcys law, on the form

$$\sigma_i = \sum_j t_{i,j} p_j,$$

where σ_i is the discrete flux over face i , $t_{i,j}$ are transmissibilities and p_j are cell pressures. The sum is taken over all cells that contribute to the flux stencil; depending on the method this may be the two cells adjacent to the face, or more cells. Details on a specific control volume method will be given in the next section. Assembly for all faces yields a global linear system to be solved for the cell pressures.

The flux discretization for a multi-phase simulation is based on pre-computing transmissibilities from the single phase pressure equation. In the time stepping scheme, the mobilities are introduced as scaling factors to the transmissibilities for each face [5]. The transport scheme, as commonly defined for scalar mobilities, can thus be written on the form

$$(7) \quad \frac{\partial \mathbf{S}_\alpha}{\partial t} - \nabla \cdot (\bar{\lambda}_\alpha \cdot \mathbf{T}_K \mathbf{p}) = \mathbf{Q}_\alpha,$$

where \mathbf{S}_α , \mathbf{p} and \mathbf{Q}_α are vectors of cell saturations, pressures and sources, $\bar{\lambda}$ are face mobilities, and \mathbf{T}_K is a transmissibility matrix, computed from the intrinsic permeability. A discrete pressure equation can be found by summing the transport equations for the two phases. To avoid artificial smearing, $\bar{\lambda}$ is usually evaluated using the value in the upstream cell, both in the pressure and in the transport equation. Possible difficulties in identifying stagnation points in cases of counter-current flow are avoided by evaluating the upstream direction for each phase separately.

As seen from Equation (7), for a scalar relative permeability, the mobility gives only a scaling of the single phase flux. When the relative permeability is a tensor, both a scaling and a rotation of the flow field are possible. To get an accurate representation of the flow field, this must be taken into account. As the product $\mathbf{T}_K \mathbf{p}$ (the single-phase flux) gives one scalar for each edge, a tensor relative permeability cannot be introduced after having calculated the transmissibilities. This implies that the calculation of transmissibilities can no longer be done in a pre-processing step due to the dependence of the relative permeability on saturation. If upstreaming is applied to the mobilities, the product between an upstream relative permeability and a downstream intrinsic permeability need not be positive definite, and the upstreaming should be applied to the saturations instead [25]. Moreover, unless the effective and intrinsic permeability have the same principal axis, the saturation dependency of the anisotropy directions can introduce counter-current flow, and the upstream direction cannot be decided based on potentials from the old time step [25].

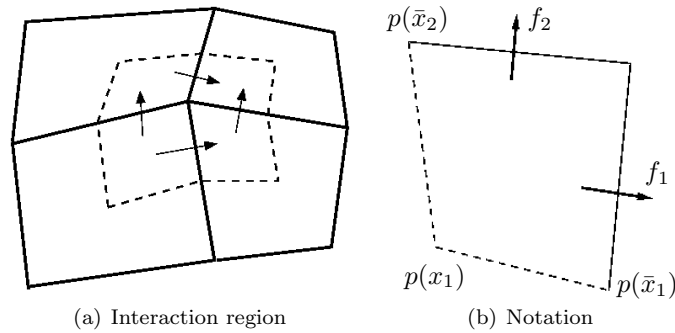


FIGURE 4. To the left, an interaction region for the MPFA O(0) method. To the right, notation used to describe the MPFA method.

It is clear from the preceding discussion that the traditional discretization methods both for the pressure and transport equations must be modified to incorporate tensorial relative permeabilities. This challenge is the main motivation of the current paper, and provides the justification for the new methods presented in Section 4. In the remainder of this section, we will review background material that is essential in order to understand the later developments.

3.2. Multi-point flux approximation methods. To get schemes with better consistency and convergence properties than the two-point flux approximation (TPFA) method, the multi-point flux approximation (MPFA) methods were introduced in the middle of the nineties. We will review the MPFA O-method here; more specifically the MPFA O(0) method, that uses the mid-points of the faces in the construction of pressure gradients. We will emphasize the points important for the schemes developed in the next subsections that allow for tensorial relative permeabilities. For more details on the MPFA methods see e.g. [1, 14].

The MPFA O-method has its name from the shape of the interaction region that is centered on each grid node as illustrated by the dashed line in Figure 4(a). The building blocks of an interaction region are sub-cells formed by connecting the centers of the cells with the mid-point of the faces of the cells. The arrows indicate the partial fluxes that are calculated with this particular interaction region.

For each sub-cell in an interaction region we construct a linear pressure gradient by using the pressure points at the center of the cell and the mid-point of each face.

The fluxes over the half-faces in a sub-cell are then given by (see Figure 4(b) for notation):

$$(8) \quad \begin{pmatrix} f_1 \\ f_2 \end{pmatrix} = \mathbf{A}^T \mathbf{K} \mathbf{B}^{-1} \begin{pmatrix} p(x_1) - p(\bar{x}_1) \\ p(x_1) - p(\bar{x}_2) \end{pmatrix}.$$

Here the matrix \mathbf{B} contains the distances between the pressure points so as to construct a linear gradient, \mathbf{K} is the permeability tensor for the cell, and \mathbf{A} is a matrix containing the integrated normals of the corresponding half-faces. By imposing continuity of fluxes, it is possible to obtain the pressures on the half-sides, $p(\bar{x}_i)$, in function of the pressures in the centers of the elements, $p(x_i)$. The pressures at the interfaces are in this way eliminated as unknowns. We then obtain the half-side fluxes as functions of only the pressure in the centers of the elements.

The fluxes over each side of a control volume (cell) are obtained by summing the corresponding half-side fluxes. We have here presented the method only in 2D, but the extension to 3D is straight forward.

4. Proposed Numerical Discretizations

As illustrated in the previous section 3.1, traditional numerical methods cannot be applied to simulate problems with tensorial relative permeabilities. In this section, two novel approaches to tackle full tensor effects are introduced. Another numerical scheme is introduced in [25], where the flux is divided into an advective part and a capillary part. Each of these are carefully analyzed to identify the correct upstream direction, and this may require up to 7 transmissibility calculations for each time step. Also, upstreaming is applied to saturations instead of mobilities. Compared to the method proposed in [25], the scheme introduced in Section 4.1 is computationally much cheaper but also less accurate for general problems, while the method presented in Section 4.2 is conceptually closer related to standard numerical methods, but it hinges on the availability of an advanced Riemann solver.

4.1. Weighted Face Mobility Approximation (WFMA). The following approach aims to be able to handle tensor relative permeability while at the same time calculating the transmissibilities in a pre-processing step. The method will therefore be computationally cheap (or relatively so), and permits the use of existing MPFA code with only minor modifications.

The key concept in WFMA is to first associate a (scalar) mobility value for each face of the cell. This means that for any face we have two values associated, one for each adjacent cell (as in the scalar case). This brings the equation back to the form (7) with scalar face mobilities, and standard solution techniques can be applied.

To obtain a scalar mobility for each face of the cell we use a weighted average of the entries in the mobility tensor. The weights are calculated using grid information and the intrinsic permeability tensor. The weights are therefore independent of the saturation and can be calculated in a pre-processing step. We will only consider the 2D case.

As seen earlier, with the MPFA O-method the half-side fluxes are calculated by Equation (8). If we insert the total mobility as in Equation (5), we have

$$\begin{pmatrix} f_1 \\ f_2 \end{pmatrix} = \mathbf{A}^T \mathbf{\Lambda}_T \mathbf{K} \mathbf{B}^{-1} \begin{pmatrix} p(x_1) - p(\bar{x}_1) \\ p(x_1) - p(\bar{x}_2) \end{pmatrix}.$$

We would like to approximate the latter with the following expression

$$(9) \quad \begin{pmatrix} f_1 \\ f_2 \end{pmatrix} = \tilde{\mathbf{\Lambda}} \mathbf{A}^T \mathbf{K} \mathbf{B}^{-1} \begin{pmatrix} p(x_1) - p(\bar{x}_1) \\ p(x_1) - p(\bar{x}_2) \end{pmatrix},$$

where $\tilde{\mathbf{\Lambda}}$ is a diagonal matrix that approximates the effect of the total mobility. Note that Equation (9) is a flux expression on the form of (4). Examining the matrix products, we note that the desired approximation can be expressed in the form (setting $\tilde{\mathbf{\Lambda}} = \text{diag}(\tilde{\Lambda}_1, \tilde{\Lambda}_2)$)

$$(10) \quad \tilde{\mathbf{\Lambda}} \mathbf{A}^T \mathbf{K} \mathbf{B}^{-1} = \begin{pmatrix} c_{11} \tilde{\Lambda}_1 & c_{12} \tilde{\Lambda}_1 \\ c_{21} \tilde{\Lambda}_2 & c_{22} \tilde{\Lambda}_2 \end{pmatrix},$$

and similarly, the 'real' discretized system can be expressed as a general linear combination of the total mobility function

$$(11) \quad \mathbf{A}^T \boldsymbol{\Lambda}_T \mathbf{K} \mathbf{B}^{-1} = \begin{pmatrix} M_{1,1} & M_{1,2} \\ M_{2,1} & M_{2,2} \end{pmatrix},$$

with

$$\begin{aligned} M_{1,1} &= d_{11} \Lambda_{T,11} + d_{12} \Lambda_{T,12} + d_{13} \Lambda_{T,21} + d_{14} \Lambda_{T,22}, \\ M_{1,2} &= d_{21} \Lambda_{T,11} + d_{22} \Lambda_{T,12} + d_{23} \Lambda_{T,21} + d_{24} \Lambda_{T,22}, \\ M_{2,1} &= d_{31} \Lambda_{T,11} + d_{32} \Lambda_{T,12} + d_{33} \Lambda_{T,21} + d_{34} \Lambda_{T,22}, \\ M_{2,2} &= d_{41} \Lambda_{T,11} + d_{42} \Lambda_{T,12} + d_{43} \Lambda_{T,21} + d_{44} \Lambda_{T,22}. \end{aligned}$$

Assuming that the functions $\tilde{\Lambda}_i$ can be well represented by a combination of the components of the mobility function, we write

$$\tilde{\Lambda}_i = w_{i1} \Lambda_{T,11} + w_{i2} \Lambda_{T,12} + w_{i3} \Lambda_{T,21} + w_{i4} \Lambda_{T,22}.$$

The weights are now the critical parameter functions to be determined. By comparing Equations (10) and (11), we see that there are more constraints (sixteen) than there are free parameters (eight). The choice is therefore neither unique nor capable of satisfying all the constraints. It is clear though that the weights will be influenced by the entries in the matrices \mathbf{A} , \mathbf{B} and \mathbf{K} . An additional consideration is that the fluxes in Equation (9) are half-face fluxes and will be summed to obtain the fluxes over the whole face. The application of weights may therefore be used before or after the assembly of the half-side fluxes. As the transmissibilities are in the end calculated for the fluxes (and not the half-side fluxes), it is more convenient to obtain a scalar total mobility for each side. After having calculated the weights for each half side we therefore use the average to obtain the weights for each side. This means that all the weights are divided by a factor of 2.

It is important to choose a set of weights so that the scalar case is represented correctly. This will not influence the weights w_{i2} and w_{i3} , as these would multiply entries that are equal to zero. The sum of the weights w_{i1} and w_{i4} should on the other hand be equal to unity (when not considering the factor 1/2).

We suggest the following choice of weights which is exact for the scalar case and should be a balanced approximation in the other cases:

$$w_{1j} = \frac{1}{2} \frac{d_{1j} + d_{2j}}{c_{11} + c_{12}} \quad \text{and} \quad w_{2j} = \frac{1}{2} \frac{d_{3j} + d_{4j}}{c_{21} + c_{22}}.$$

In addition we limit the weights such that they are comprised between 0 and 1. This is to avoid that the weights overcompensate for the lack of off-diagonal terms in $\tilde{\mathbf{A}}$. We note that the choice of weights is by no means obvious. Indeed, apart from reproducing the scalar relative permeability case, the only other criteria is to limit excessive grid orientation effects.

In the special case where the grid is a parallelogram, $\mathbf{B}^{-1} = \mathbf{A}$ and the weights reduce to

$$w_{11} = \frac{1}{2}, \quad w_{12} = \frac{1}{2} \frac{k_{22}}{k_{11}}, \quad w_{13} = w_{14} = 0,$$

and

$$w_{21} = w_{22} = 0, \quad w_{23} = \frac{1}{2} \frac{k_{11}}{k_{22}}, \quad w_{24} = \frac{1}{2}.$$

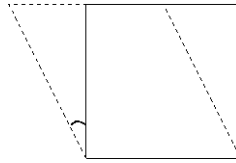


FIGURE 5. Set-up for testing grid effects for the choice of weights

The WFMA method can be summarized as follows:

Algorithm - Weighted Face Mobility Approximation

Prior to the time stepping, compute the weighting functions w_{ij} so that a scalar relative permeability can be computed for each face.

Then, for each time step:

- (1) Solve the pressure equation (5) using upstream mobilities.
- (2) Compute fluxes over faces.
- (3) Propagate saturations using upstream mobilities.

To illustrate grid orientation effects for this choice of weights, we consider the approximations for a single subcell for a varying degree of grid skewness. The intrinsic permeability is set to unity, while we consider two relative permeability tensors: Both have an anisotropy ratio of 5:1; with the major axis aligned with and rotated 30° from the x -axis, respectively. The initial configuration of the subcell is a square. We then rotate the vertical lines from 0° of the initial position up to 45° . See Figure 5 for an illustration. The first relative permeability considered will therefore always have one principal axis aligned with the grid, as the horizontal lines are kept fixed. This is not so for the second test case. To measure the deviations, we compute the components of the tensors in Equation (10) and (11), and plot the quantity

$$T_{ij} = \frac{|N_{ij} - M_{ij}|}{M_{ij}},$$

N_{ij} referring to the elements in (10). The differences are shown in Figure 6. We see that when the relative permeability has one principal axis aligned with the grid, the errors are relatively small, and the elements N_{21} and N_{22} are exact. In these cases we can expect fairly good results with WFMA. In the case were the relative permeability tensor is rotated with respect to the grid, all components are approximated. In particular we note that the component T_{21} is not captured at all. Since the weights are independent of the relative permeability, this example indicates that the WFMA approach cannot be expected to predict the flow pattern for any type of grid orientation. Other choices of weights will have the same limitations.

One may compare this case with the single phase simulation on a grid that is not \mathbf{K} -orthogonal: It is still possible to capture some of the flow pattern using the TPFA method, but for a correct modeling of the anisotropy effects of the intrinsic permeability the MPFA method should be used. It has indeed been proven that the TPFA method converges to the wrong solution in such cases, see [2].

Directional dependency of the relative permeability often arises in two-phase upscaling. For the idealized cases presented in Section 2, the upscaled parameters

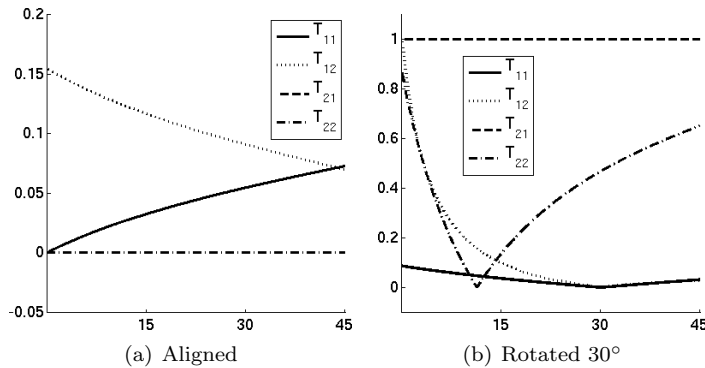


FIGURE 6. The approximations of the WFMA approach. T_{ij} represents the difference in the tensor components, relative to the size of the full tensor elements. To the left, $\mathbf{\Lambda}$ is aligned with a Cartesian grid, to the right, the tensor is rotated 30° . In the left figure, the T_{21} and T_{22} elements are coinciding.

could be calculated analytically. However, for more realistic media numerical techniques are necessary, e.g. [10, 24]. In such cases, a relative permeability function is usually computed for each face in the coarse grid, in effect projecting the upscaled tensor onto the faces. This makes treatment of the mobility tensor in the coarse simulations trivial. WFMA can be seen as a generalization of this approach in that it computes a scalar quantity for each face, even if the tensor is not aligned with the grid. We remark that two-phase upscaling to a full effective permeability was considered in [22].

4.2. Full tensor discretization (FTD). The face-based method (WFMA) described in the preceding section can be considered a way to introduce tensorial relative permeability with only minor modifications to standard discretization methods. This makes the methodology attractive, e.g. for legacy codes. However, the strategy cannot be expected to yield accurate results in all situations, as the approach does not honor the principal directions of the relative permeability. In this section, a method that aims to simulate general tensors consistently is presented.

As discussed in Section 3.1, a new discretization of Equation (5) is needed for each time step to honor saturation dependency in the permeability. A unique upstream direction need not exist for each face, thus upstream weighting of the mobility is not always possible. Instead, a cell representation of the relative permeability is used; in the terms of Section 3.1, we compute transmissibilities on the form $\mathbf{T}_{\mathbf{\Lambda}_T \mathbf{K}}$. That is, generalized harmonic averaging of the total (not phase) mobility is applied. There might be some smearing due to the harmonic averaging of fluid properties, however, we do not expect severe difficulties when applied to the pressure equation only. This approach is consistent with the general understanding of discretization of the single-phase pressure equation [11].

The transport scheme can be based on the fractional flow formulation and the total velocity field, i.e. on Equation (6). Moreover, the hyperbolic nature of the transport equations means the mobilities should be evaluated in the upstream direction to limit smearing of the saturation. The phase flow field need not be aligned with the total velocity, and it is crucial that rotations represented in the product $\mathbf{\Lambda}_\alpha \mathbf{\Lambda}_T^{-1}$ are captured by the transport scheme. When discretizing the pressure

equation by a control volume method, we compute only the normal component of the velocity field on each face. Thus, a velocity field inside the cells must be constructed to compute the transport over each face. One possibility is to apply reconstructions designed for streamline methods (see for instance [13]). In this work, we have instead used the following approach: The face pressures are reconstructed from pressures in the cell centers. From this, a pressure gradient is constructed on each sub-cell (if the pressure equation was discretized by an MPFA method, this reconstructed pressure gradient can be obtained consistently with the numerical pressure solution). A total velocity field on a sub-cell is then found as

$$\mathbf{q}_T^{sub} = -\mathbf{\Lambda}_T \mathbf{K} \nabla p^{sub},$$

with the properties that the normal component is continuous over the half-faces (and equal to the value obtained from the pressure discretization), whereas the tangential components are different on the two sides of the faces. The velocities are, however, consistent with the sub-cell pressure fields from the pressure discretization.

Now, the flux function for the phase from each side of the half face is found as the product

$$f_\alpha(S) = \mathbf{n} \cdot (\mathbf{\Lambda}_\alpha(S) \mathbf{\Lambda}_T^{-1}(S) \mathbf{q}_T^{sub}(S)).$$

This is a Riemann problem, where the flux function in general is discontinuous over the half face. After assembly over all half faces, the transport equation (6) can be solved. Note that since the phase flux over a face can be larger than the total flux (if $\mathbf{n} \cdot (\mathbf{\Lambda}_\alpha \mathbf{\Lambda}_T^{-1} \mathbf{q}_T^{sub}) > \mathbf{n} \cdot \mathbf{q}_T^{sub}$), tensorial relative permeabilities can lead to counter-current flow.

To capture tensor effects, a description of the full velocity field inside the cells are needed. With the current formulation of FTD, this is obtained by using the sub-cell gradients from MPFA. For common applications of MPFA, accurate representations of the projection of the gradient onto the normal of the faces, and thereby accurate velocity fields, are crucial. Finite volume schemes aim to calculate fluxes accurately, not gradients, and the tangential component of the velocity is normally of less importance, and it is known to be less accurate. First order convergence of the flux has been proved, also on general grids [19], while the accuracy of the tangential component is not assured. However, a reconstructed gradient based on the MPFA O-method has been shown to converge weakly to the actual gradient [4]. An inaccurate sub-cell velocity will reduce the accuracy of the FTD approach, and better representations of the tangential components of the subcell velocity field is therefore a topic for further research.

Since \mathbf{q}_T^{sub} is time dependent, our only knowledge a priori to the simulation is that the flux function will be some linear combination of the elements in the fractional flow tensor $\mathbf{\Lambda}_\alpha(S) \mathbf{\Lambda}_T^{-1}(S)$. Furthermore, the tangential component of the velocity field will not be continuous at discontinuities in the tensor field. Such discontinuities can be introduced by heterogeneities in $\mathbf{\Lambda}$ and \mathbf{K} themselves, but also by a homogeneous $\mathbf{\Lambda}$ if the saturation is discontinuous. Thus, unless the principal axes of the effective permeabilities in the two adjacent cells are coinciding, the flux function over an edge will be discontinuous.

Algorithm - Full Tensor Discretization

For each time step:

- (1) Solve the pressure equation (5) using cell centered relative permeabilities.

- (2) Compute fluxes over half faces, and reconstruct a full velocity field inside the cells.
- (3) Propagate saturations by solving discontinuous Riemann problems for each face.

The FTD scheme hinges on an appropriate Riemann solver for computing the transport over each edge. Solving Riemann problems with discontinuous flux functions is a topic that is not yet fully understood. For porous media flow, such problems arise for instance when the relative permeability is heterogeneous (see e.g. [16, 18]). When gravitational forces are present, phase by phase evaluation of the upstream direction may not yield a convergent scheme [3], and more care must be taken to get the correct flux over cell faces. Much work has been done to find both exact and approximate solutions to Riemann problems with various shaped flux functions, see [3, 9] and the references therein. Since the tensor components in the relative permeability may be quite general, a larger variety of flux functions can be expected compared to the traditional S-shaped functions (possibly with local max/min-points induced by gravity); the off-diagonal elements in the relative permeability tensor can yield much more complex shapes. In the present work, simple upstream weighting is applied for cases where the flux functions are monotone for both sides of the edges. In Section 5.2, the Engquist-Osher method in [9] is used as well. We note that from a mathematical point of view, neither existence nor uniqueness of the solution to a general Riemann problem is guaranteed. Even though the scheme will benefit from a better understanding of analytical and numerical approaches to Riemann problems, it is our experience that the FTD approach is applicable for the parameter functions discussed herein.

The scheme described above is designed to capture the full effect of tensorial relative permeabilities. The method can be shown to be consistent, under assumptions that the pressure and transport discretizations are second and first order accurate, respectively, and that the pressure equation is solved on a fine enough grid compared to the transport grid. Contrary to standard IMPES-schemes, the discrete pressure equation cannot be derived as a sum of the transport discretizations, leading to less consistency in how the terms in the equations are handled. This has not caused difficulties in our experiments. Moreover, in the MPFA discretization needed in each time step one matrix must be inverted for each node in the grid. The matrices are usually small (for Cartesian grids in 2D and 3D, respectively), and the process is trivially parallelized; nevertheless, the computational cost is higher compared to the WFMA scheme. However, the harmonic averaging means that the upstream direction is always well defined.

To sum up, the FTD scheme is a consistent approach to simulate full tensor effects. The MPFA discretization for each time step means the pressure equation is based on the actual medium conductivity. In the transport solve, saturation dependent rotations are captured, and the scheme honors possible discontinuities in the velocity field. The methodology should therefore be a robust approach to simulating full tensor problems.

5. Numerical experiments

In this section, we present two numerical experiments. The simulations serve a dual purpose. Firstly, they illustrate special flow effects that cannot be captured with scalar relative permeabilities. Secondly, they indicate properties of the numerical approaches presented in Section 4.

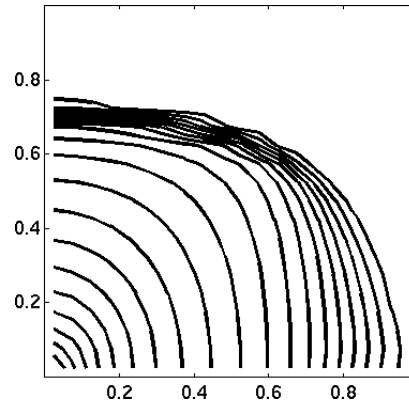


FIGURE 7. Upscaled saturation profile from a simulation on the fine scale layered model.

To the best of our knowledge, no analytical solutions are available for problems with tensorial relative permeabilities. Our numerical experiments will therefore be motivated by the upscaling examples given in Section 2.2 and 2.3. In both cases, upscaling yields a tensorial relative permeability, and a fine scale reference solution can be used to evaluate the quality of the numerical solutions.

5.1. A layered medium. This experiment is based on the upscaling example described in Section 2.2. For the fine model, we consider a medium with constant properties in the x -direction, while in the y -direction the two media described in Section 2.2 are alternating. The width of the layers is uniform, and there are in total 60 pairs of layers (i.e. 120 individual layers) in the domain. Our coarse grid is logically Cartesian, with 20×20 cells, thus the upscaling gives three pairs of layers within each coarse cell.

Initially, the medium is filled with oil. We inject water in the lower left corner of the grid at a constant rate, and produce oil at a fixed rate in the upper right corner. The viscosity ratio is set to $\mu_o/\mu_w = 10$ and the porosity is homogeneous. For further information on the setup, see Section 2.2, and also Figure 2.

To illustrate which effects we can expect from the physical model, we first show results from simulations on the fine scale. The computational grid here is Cartesian, with 100×600 cells, rendering a fine discretization of each of the individual layers. The injection rate is low enough for the capillary forces to be important, mimicking the assumptions for the upscaling in Section 2.2. However, to keep the computational cost reasonable, capillary forces are not fully dominating. This will lead to some discrepancies between the results from the fine scale solution and those of the coarse simulations.

Figure 7 shows a representative saturation distribution upscaled (after simulation) to the coarse grid. We note that the intruding water cannot propagate freely in the y -direction. In each layer the saturation must exceed a threshold value before it can intrude into the next layer, thus the saturation front in the y -direction is quite steep. In contrast, there are no capillary barriers in the x -direction, and the water propagation is faster, with a profile similar to what one will expect for injection of a less viscous fluid.

First we focus on the modeling capabilities of tensor relative permeabilities. Figure 8 shows the saturation profile obtained by the two approaches, computed

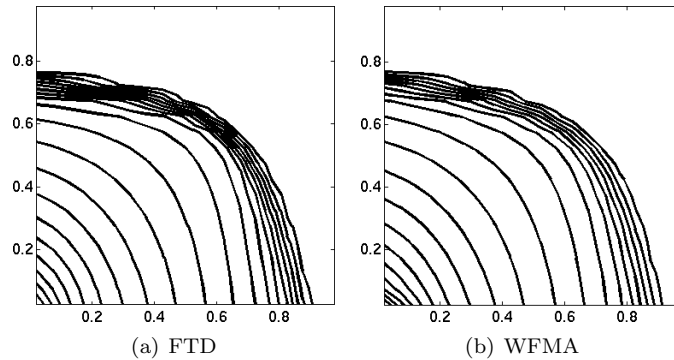


FIGURE 8. Saturation profiles obtained at time 0.25 PVI by the FTD and WFMA approaches. The simulations are performed on the upscaled model.

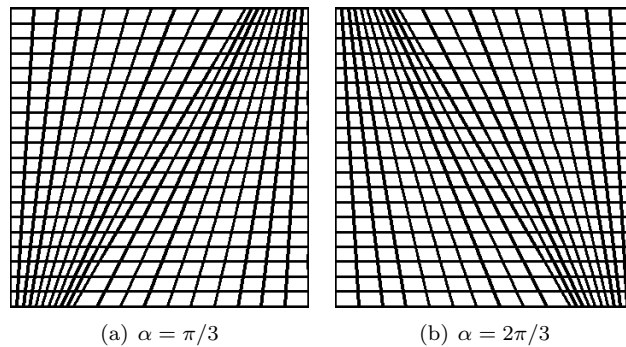


FIGURE 9. Skewed grids used in the simulations

on a coarse Cartesian grid. Both saturation fields are shown at 0.25 pore volumes injected (PVI). Since both the intrinsic and the relative permeability tensors are aligned with the grid, both the FTD and the WFMA approach reduces to two-point fluxes, and yield very similar results. We note similar features to those of the fine scale simulation: The water propagation is fastest in the x -direction, and the propagation in the y -direction is constrained by the capillary barrier effect, which in the upscaled simulation is modeled by the relative permeability. For a model with homogeneous relative permeability and capillary pressure, these effects are unique for directional dependent relative permeabilities. The position of the front is also in good agreement with the fine scale model. We remark that all coarse simulations are performed without capillary pressure.

To investigate the robustness of the numerical methods we run the same test on deformed Cartesian grids. Figure 9 shows two logically Cartesian grids, with a maximum deformation angle of $\alpha = \pi/3$ and $2\pi/3$, respectively. The cells are general quadrilaterals, and the principal directions of the relative permeability tensor are no longer aligned with the grid. The coarse simulations are again run on a 20×20 grid with both the FTD and the WFMA methods.

The saturation profiles for FTD are shown in Figure 10. We notice some discrepancies between the results, and that the Cartesian simulations (corresponding

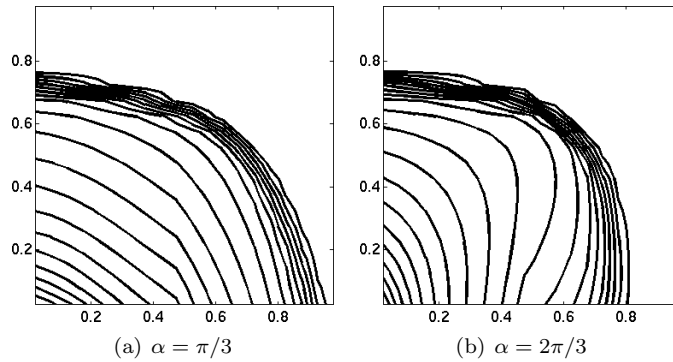


FIGURE 10. Saturation profiles obtained at time 0.25 PVI by the FTD approach. The simulations are performed on skewed grids.

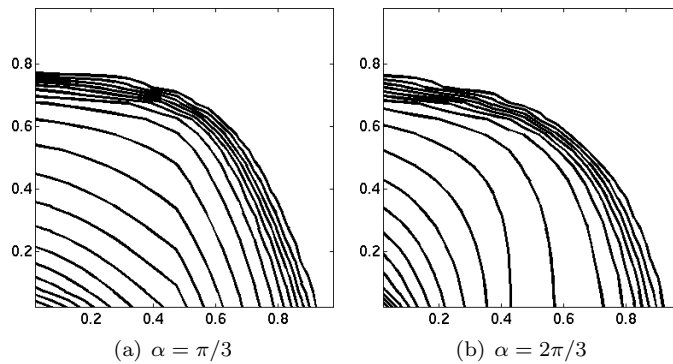


FIGURE 11. Saturation profiles obtained at time 0.25 PVI by the WFMA approach. The simulations are performed on skewed grids.

to $\alpha = \pi/2$) gives an intermediate saturation profile. The origin of this grid orientation effect may be due to the reliance on the MPFA sub-element gradients and in particular the accuracy of the tangential components (see Section 4.2). The overall effect is still well represented though, with a constrained propagation in the y -direction.

Saturation profiles obtained by the WFMA method on the skewed grids are shown in Figure 11. In this case, the projection strategy works well. Although there are some grid orientation effects away from the front, the front location in itself is fairly invariant to the changing grid.

5.2. Tensor with rotations. In the previous section, we considered tensor effects both on grids that were aligned with the tensor and on skewed grids. For both cases, the principal directions of the tensor were independent of the saturation. In this section, we will consider tensors where the principal directions rotates as a function of saturation. The setup is based on the vertical equilibrium upscaling shown in Section 2.3.

We first present a simulation on the full 3D model. The domain is a $30 \times 30 \times 30$ Cartesian grid on the unit cube. To avoid the singularity in the intrinsic permeability at the bottom of the formation, the horizontal cell permeabilities are found

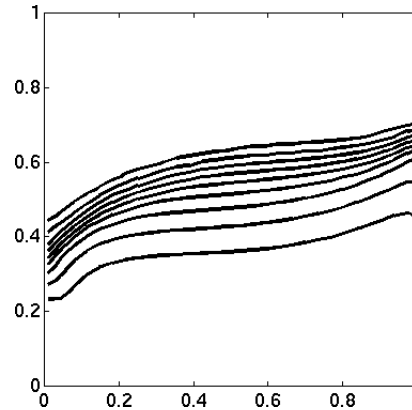


FIGURE 12. Saturation profile from a simulation of the full 3D model at $t = 0.5$ PVI. The figure shows vertically averaged saturations in the xy -plane.

by evaluating Equation (2) in the cell centers, with $(\gamma_1, \gamma_2) = (1, 0.8)$. Note that this means the extreme anisotropy at the very bottom of the formation is not captured in the 3D model (cf Figure 3), thus we expect the 3D simulation to somewhat underestimate the rotation of the saturation front. The vertical permeability is set to unity. The relative permeabilities for both phases are linear, corresponding to vertical segregation within each cell. To get vertical segregation of the two phases, a large density difference is preferable. However, this would have led to a large capillary pressure in the upscaled model (see e.g. [20]), which the FTD model is currently not formulated to handle. Therefore, the density difference is set to $\rho_o/\rho_w = 0.8$. The viscosity ratio is unity. To get an injection scheme consistent with vertical segregation, we inject water along the axis ($y = 0, z = -H$), that is, at the bottom of the formation.

As suggested by Figure 3, the flow of the water phase will be to the right compared to the average flow direction, with the strongest rotation for low saturations. The vertically averaged saturation profile from a full 3D simulation at time 0.5 PVI is presented in Figure 12. We see a clear preferential flow of the water saturation toward the right side of the domain.

Next, we simulate the same flow scenario on the upscaled (2D) medium, on a 30×30 Cartesian grid. We will consider both a homogeneous case (the same as for the 3D simulation), and a heterogeneous field, defined by:

Case A:

$$\mathbf{K}_w = \mathbf{K}_r(S; \gamma_1 = 1, \gamma_2 = 0.8).$$

Case B:

$$\mathbf{K}_w = \begin{cases} \mathbf{K}_r(S; \gamma_1 = 1, \gamma_2 = 0.8) & x < 0.5, \\ \mathbf{K}_r(S; \gamma_1 = 1, \gamma_2 = -0.1) & x > 0.5. \end{cases}$$

Here, \mathbf{K}_r refers to Equation (3). In Case A, the water should tend to flow to the right throughout the domain as discussed, while in Case B, the water flow will be towards the center of the domain where the discontinuity lies, with a significantly stronger rotation in the left half of the domain. The numerical values of γ_2 are selected to highlight this behavior.

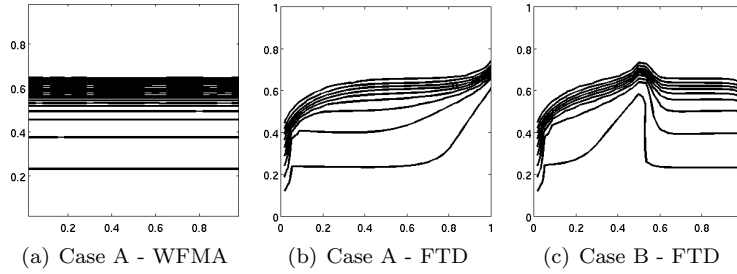


FIGURE 13. Left and middle: Saturation profiles for Case A and B, respectively. The saturation profiles are shown at $t = 0.5$ PVI. To the right, the transport over the edge $x = 0.5$ (cross the main flow direction) at $t = 0.5$ PVI.

We first examine the results obtained by using the WFMA method for Case A. As seen in Figure 13(a), the weights are not sufficient to pick up any rotation in the fluid and the solution is independent of x . The result for Case B presents the same uniform front and is therefore not included. We conclude that for cases where the principal directions of the relative permeability tensor are dependent on saturation the WFMA method cannot be relied upon to produce an accurate saturation profile.

For the FTD method the results are presented in Figure 13. Figure 13(b) shows the saturation profiles at 0.5 PVI for the homogeneous Case A. We see the expected net transport toward the right boundary. For the low saturations near the front (corresponding to areas with high anisotropy in the 3D model), a strong cross-flow can be seen as the fluid piles up at the right boundary of the domain. The effect of the relative permeability can also be seen in the leftmost grid column, where the wetting phase flows out of the right faces without a recharge from the left edge, leading to a lag in saturation values. Comparing with Figure 12, we see that the FTD results are in good agreement with the 3D simulations.

The results from Case B is shown in Figure 13(c). Since in the left part of the domain is equal to the value used in Case A, the saturation profiles are also very similar. In the other half of the domain, the relative permeability stems from a 3D formation with less heterogeneity in the intrinsic permeability and the saturation experience only a minor rotation effect. Again, the FTD approach produce reasonable results.

Finally, we consider the accuracy of the FTD scheme for a full tensor problem on increasingly fine grids. The lack of analytical solutions for problems with tensorial relative permeabilities makes traditional convergence tests unfeasible. We therefore resort to comparing solutions obtained on a coarse grid with a reference solution, computed by FTD on a 256×256 Cartesian grid. The simulations are run to $t = 0.5$ PVI, and the coarse solutions are mapped onto the fine grid using constant interpolation. The norm of the differences are then computed according to

$$\|s_h - s_{\text{ref}}\| = \sum_i V_i |s_h^i - s_{\text{ref}}^i|, \quad \|p_h - p_{\text{ref}}\| = \sum_i V_i |p_h^i - p_{\text{ref}}^i|^2,$$

V_i representing cell volumes. The results are shown in Figure 14. They indicate first and second order convergence for the saturation and pressure, respectively. This is

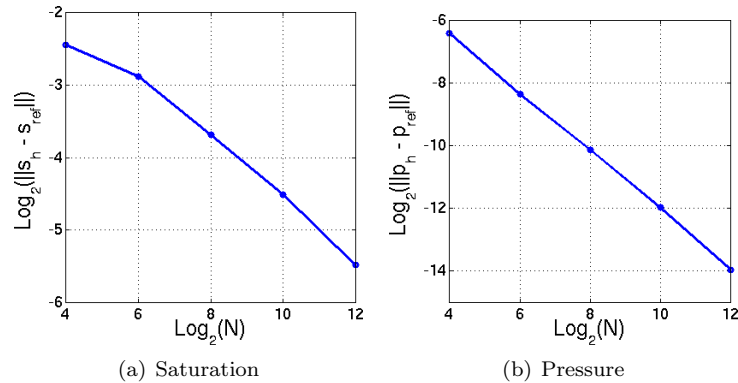


FIGURE 14. Convergence of the pressure and saturation profiles towards a fine grid reference solution. Both solutions are taken at $t = 0.5$ PVI. The grid is Cartesian, and the number of cells is denoted by N .

in accordance with the order of accuracy for the transport and pressure solver (e.g. [1, 8]), and the test gives an indication that the FTD scheme is self consistent.

6. Concluding remarks

In this contribution we have investigated saturation dependent full tensor descriptions of fluid mobility in porous media. While commonly neglected in practical modeling and simulation, we have shown how the full tensor descriptions naturally appear at the REV scale, and through upscaling. Notably, we have illustrated the physical mechanisms by which both the ratio as well as the main directions of anisotropy can be dependent of saturation.

Saturation dependent full tensor mobilities invalidate common simplifications used to create efficient numerical implementations for the equations of fluid motion in porous media. This holds true for discretizations of both the so-called pressure and saturation equations. Here, we propose two strategies to overcome current limitations. The first strategy, termed WFMA, is appropriate in order to allow existing codes to accommodate for relative permeability which primarily emphasizes existing directions in the grid and intrinsic permeability. The second strategy is an approach to consistent discretization of both the pressure and the saturation equations in the presence of a relative permeability which has saturation dependent directions of anisotropy.

Numerical results have been presented that support the design properties of our strategies. This allows draw the following conclusions: Firstly, upscaled models with anisotropic relative permeability are qualitatively consistent with their fine scale equivalents; Secondly, anisotropic features of relative permeability can partially be included in existing simulation software at low computational overhead; Finally, our proposed numerical scheme for full relative permeability models handles both saturation-dependent scaling and rotation of relative permeability, with low grid-orientation effects.

Two of the main obstacles to widespread applications of full descriptions of relative permeability models remain good numerical methods and a lack of measurements. While this paper represents a contribution to tackle the first of these obstacles, we acknowledge that the final word on this issue has not been said.

Acknowledgments

The simulations presented in Section 5 were implemented in part using components of the Matlab Reservoir Simulation Toolkit (MRST), available online at <http://www.sintef.no/Projectweb/MRST/>.

References

- [1] I. Aavatsmark. An introduction to multipoint flux approximations for quadrilateral grids. *Comput. Geosci.*, 6(3-4):405–432, 2002.
- [2] I. Aavatsmark. Interpretation of a two-point flux stencil for skew parallelogram grids. *Comput. Geosci.*, 11(3):199–206, 2007.
- [3] Adimurthi, J. Jaffré, and G.D. Veerappa Gowda. Godunov-type methods for conservation laws with a flux function discontinuous in space. *SIAM J. Numer. An.*, 42(1):179–208, 2004.
- [4] L. Agelas and R. Masson. Convergence of finite volume mpfa o type schemes for heterogeneous anisotropic diffusion problems on general meshes. *C. R. Acad. Sci. Paris*, 246:1007–1012, 2008.
- [5] K. Aziz and A. Settari. *Petroleum Reservoir Simulation*. Chapman & Hall, 1979. ISBN: 0-85334-787-5.
- [6] S. Bakke and P. E. Øren. 3-d pore-scale modelling of sandstones and flow simulations in the pore networks. *SPE J.*, 2:136149, 1997.
- [7] J. Bear, C. Braester, and P. C. Meiner. Effective and relative permeabilities of anisotropic porous media. *Transp. in Porous Media*, 2:301–316, 1987.
- [8] Yann Brenier and Jérôme Jaffré. Upstream differencing for multiphase flow in reservoir simulation. *SIAM J. Numer. Anal.*, 28(3):685–696, 1991.
- [9] R. Burger, K. H. Karlsen, and J. D. Towers. An Engquist-Osher-type scheme for conservation laws with discontinuous flux adapted to flux connections. *Siam J. Num. An.*, 47(3):1684–1712, 2009.
- [10] Y. Chen and Y. Li. Local-global two-phase upscaling of flow and transport in heterogeneous formations. *Multiscale Model. Simul.*, 8(1):125–153, 2009.
- [11] Z. Chen and Y. Huan, G. and Ma. *Computational methods for multiphase flows in porous media*. Computational Science & Engineering, SIAM, Philadelphia, PA, 2006. ISBN: 0-89871-606-3.
- [12] A. Corey and C. H. Rathjens. Effect of stratification on relative permeability. *Petrol. Trans. AIME*, pages 358–360, 1956.
- [13] A. Datta-Gupta and M.J. King. *Streamline simulation: Theory and practice*. Society of Petroleum Engineers, 2007. ISBN:1555631118.
- [14] M. G. Edwards and C. F. Rogers. Finite volume discretization with imposed flux continuity for the general tensor pressure equation. *Comput. Geosci.*, 2(4):259–290, 1998.
- [15] H. Eichel, R. Helmig, I. Neuweiler, and O. A. Cripka. Upscaling of two-phase flow processes in porous media. In *Upscaling multiphase flow in porous media: from pore to core and beyond*. Springer, 2005.
- [16] T. Gimse and N. H. Risebro. Solution of the cauchy-problem for a conservation law with a discontinuous flux function. *Siam J. Mat. An.*, 23(3):635–648, 1992.
- [17] A. G. Hunt. *Percolation theory for flow in porous media*. Number 674 in Lecture Notes in Physics. Springer, 1985.
- [18] J. Jaffre. Flux calculation at the interface between two rock types for two-phase flow in porous media. *Transp. Por. Med.*, 21(3):195–207, 1995. Times Cited: 4.
- [19] R. A. Klausen and A. F. Stephansen. Convergence of multi-point flux approximations on general grid and media. *Int. J. Num. An. Mod.*, 2011. Submitted.
- [20] L. Lake. *Enhanced Oil Recovery*. Prentice Hall, 1989. ISBN:0-13-281601-6.
- [21] J. M. Nordbotten, M. A. Celia, H. K. Dahle, and S. M. Hassanizadeh. On the definition of macroscale pressure for multiphase flow in porous media. *Wat Resour. Res.*, 44(6), 2008.
- [22] G.E. Pickup and K.S. Sorbie. The scaleup of two-phase flow in porous media using phase permeability tensors. *SPE J.*, 1(4):369–382, 1996. SPE 28586.
- [23] M. Quintard and S Whitaker. 2-phase flow in heterogeneous porous media: The method of large-scale averaging. *Transp. in Porous Media*, 3(4):357–413, 1988.
- [24] A.B. Rustad, T.G. Theting, and R. Held. Pore scale estimation, up scaling and uncertainty modeling for multiphase properties. In *Proc. of SPE/DOE Symposium on Improved Oil Recovery.*, 2008. SPE 113005.

- [25] M. Wolff, B. Flemisch, R. Helmig, and I. Aavatsmark. Treatment of tensorial relative permeabilities with multipoint flux approximation. *Int. J. Num. An. Mod.*, 2011. Submitted.
- [26] T. C. J. Yeh, L. W. Gelhar, and Gutjahr. Stochastic-analysis of unsaturated flow in heterogeneous soils. 2. statistically anisotropic media with variable α . *Wat. Resour. Res.*, 21(4):457–464, 1985.
- [27] T. C. J. Yeh, L. W. Gelhar, and Gutjahr. Stochastic-analysis of unsaturated flow in heterogeneous soils. 3. observations and applications. *Wat. Resour. Res.*, 21(4):465–471, 1985.
- [28] Y. C. Yortsos. A theoretical analysis of vertical flow equilibrium. *Transp. in Porous Media*, 18:107–129, 1995.

University of Bergen Johannes Bruns gt. 12 5008 Bergen, Norway

E-mail: Eirik.Keilegavlen@uib.no and Jan.Nordbotten@math.uib.no

URL: <http://www.uib.no/persons/Eirik.Keilegavlen> and <http://www.uib.no/People/nmajn/>

Uni CIPR, Uni Research, Allégaten 41 5007 Bergen, Norway

E-mail: annette.stephansen@uni.no

URL: <http://www.cipr.uni.no/person.aspx?person=427>